NDE2015, Hyderabad
November 26-28, 2015

X-ray Computed tomography based detection of casting defects in fatigue samples:

K. Arunmuthu[1*], *George Joseph*[2], *T. Saravanan*[1], *John Philip*[1] *and B.P.C Rao*[1]

1 RTS, NDE Division
Indira Gandhi Centre for Atomic Research
Kalpakkam-603 102, Tamil Nadu
2 BITS, Pillani
**arunmuthuk@igcar.gov.in*

Abstract

Computed tomography (CT) imaging is widely used by various industries for characterization of defect features where a three-dimensional image of an object is reconstructed from a large number of X-ray projection images taken around an axis of rotation. In the present paper, X-ray computed tomography (X-CT) is used to characterize the casting defects in the Nickel-aluminum bronze (NAB) alloy. The NAB alloys are extensively used in marine applications such as propellers, couplings and pump casings and impellers due to their good mechanical properties such as tensile strength, creep resistance, and corrosion resistance. However, there are several instances of in-service failure of these alloys due to high cycle fatigue (HCF). Before subjecting to HCF tests, the samples were subjected to X-CT for characterization of casting defects features. X-CT was carried out using a 450kV Balteau constant potential X-ray tube and flash scan FS35 Thales flat panel X-ray detector with 127 µm pixel size. Modified filtered back-projection technique is adopted to reconstruct the cross-sections and Image J software tool is used for 3-dimensional visualization of the defect features. The horizontal and vertical cross-sections reconstructed give the position and length of the defects. The nature and size of the defects observed were categorized into four group's small (~1mm), intermediate (~2mm), large (~3mm) and surface defects. Some of the small and intermediate defects were found at depths of about 2mm and 1.85 mm respectively. Analysis of the HCF data showed that the proximity of the defect features from the surface has significant influence over the size of the defects.

Keywords: Computed tomography, fatigue, HCF, filtered back projection, 3D visualization

1. Introduction

The growth of defects such as shrinkage cavities and gas pores control the fatigue life of cast materials. Fatigue properties of castings are strongly dependent on the casting defects and less affected by chemical composition, heat treatment, or solidification time [1-4]. The crack initiation stage is assumed to be negligible since fatigue cracks are usually observed early in life. To predict the fatigue life, defects are considered as pre-existent. The fatigue life and fatigue limit are controlled by the crack propagation law [5–7]. Typical casting defects formed are macro pores and micro pores [4]. The combination of complex part geometry and solidification process gives rise to different pore types and sizes in different sections of the casting. The morphology of casting pores in alloys is typically classified either as gas pore or micro shrinkage pore [1]. While the former is typically rounded and spheroidal, the latter is branched and elongated. In practice, the distinction is not always straightforward.

The accuracy of the fatigue life prediction strongly depends on the prior knowledge of the defect location and size for a given material. One of the most important parameter in determining the fatigue property of castings is the size of the largest defect detected. The larger the maximum defect size, the lower the fatigue strength. Hence, any defect tolerant design for materials should be based on a method to estimate the largest defect size distribution and procedure developed by Murakami and coworkers [8], represents a fundamental starting point in this regard.

Using nondestructive testing methods such as liquid penetrant (LPI) and magnetic particle inspection (MPI) [9] one can detect the surface opened defects while ultrasonic testing (UT) [10] and radiographic testing (RT) it is possible to measure the size and position of casting defects in cast components. Non-destructive testing (NDT) is defined as the application of inspection method to a component or structure in which the test piece is not affected by the testing method. The nuclear power industry has always had special problems and it is directly responsible for the most important development in NDT [11]. Most NDT system is designed to reveal defects such as porosity, cracks, and corrosion etc. in volumetric and surfacial aspects of any object. One of the most widely used methods is RT, due to its high reliability, versatility and ability to provide permanent information [12].

Ferrie and coworkers applied high resolution synchrotron X-CT to characterize pore in cast alloys [13]. The application of X-CT allowed the accurate non-destructive 3-D reconstruction of pores within a volume of aluminum alloy (i.e. distribution, size and morphology). X-CT was used to study the early stages of fatigue crack nucleation and growth from pores [14]. The application of X-CT in comparison to metallography on cast aluminum parts is discussed briefly in [15].

Recently, 3D X-CT is used to visualize the internal structure of materials more accurately. Computed tomography is used in several applications such as medicine, non-destructive testing/evaluation, astronomy and others to look inside the object and analyze the internal structures [16-17]. X-ray CT is suitable for inspection of complex structures of fiber composites materials, flaw detection, analysis of failure, dimensional measurement of not accessible geometrical features, inspection of assemblies, and investigation of material properties such as density distribution [18]. Hence, CT has become a unique tool to locate defects, check internal geometry in turn providing an opportunity for reverse engineering and also an excellent means for research on new materials and development of new products. Recent developments in high resolution X-CT have made possible the three dimensional characterization of porosity [19–20].

In this paper 3D tomography system is described that helps in characterization of defects in cast materials. In this research, several fatigue specimens were cut from casting blanks of dimensions 25x25x110mm made of Nickel-Aluminium-Bronze (NAB) as major constituents. The present paper aims at characterizing the casting defects in NAB alloy through RT and X-CT into distinct defect groups having particular defect size and location. The quantitative measurement capability of X-CT provides a technically superior approach for feature dimensions and material density uniformity measurements.

2. Cone Beam X-ray Tomographic System

The X-Ray tomographic systems which are in use in industry to date produce in most cases two dimensional sectional images. In such a system an X-ray fan from an X-ray source penetrates the object and the attenuation is measured by a linear detector. The object is rotated, during the rotation a set of one dimensional projections is measured and reconstructed. The result is a two dimensional image. To get a three dimensional image with such a conventional tomograph, the object has to be moved in the direction of the axis of rotation and several scans have to be performed. A stack of slices has to be mounted to get a three dimensional image. A conical beam from an X-ray source penetrates the investigated object. The attenuated radiation is measured by a large area detector (Fig. 1). In order to irradiate the object from all sides, the X-ray source and the detector are kept stationery, and the object rotates in the X-ray cone. During rotation a set of projections is measured and stored. The set of projections is then used to reconstruct the 3D structure of the object.

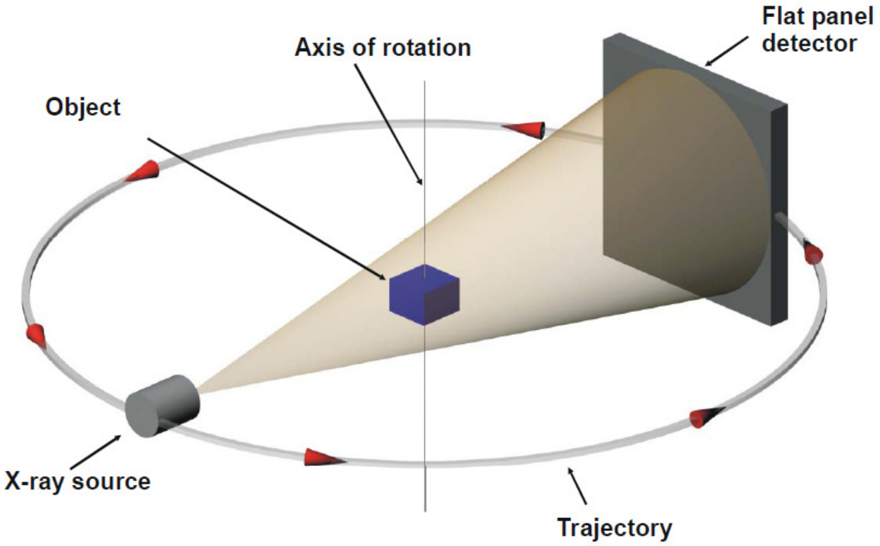

Fig. 1: Principle scheme of 3D cone-beam tomography

The advantage of cone beam tomography is besides the feature of fast volume scanning the fact that in cone beam tomography the high spatial resolution is obtained isotropically in all three directions. Therefore especially for bodies with complex inner structures 3D tomography is the appropriate inspection method. More details about the tomography system reconstruction method are presented by Herman [21-23].

3. Development of in-house X-ray Computed Tomography System

The experimental tomographic imaging system has been developed in the laboratory is described below in detail. The system consists of an X-ray source, Flat panel detector and a computerized scanning mechanism and related instrumentation. Figure 2 shows the CT system developed in the laboratory and the specification of the in-house developed CT system is given in Table 1.

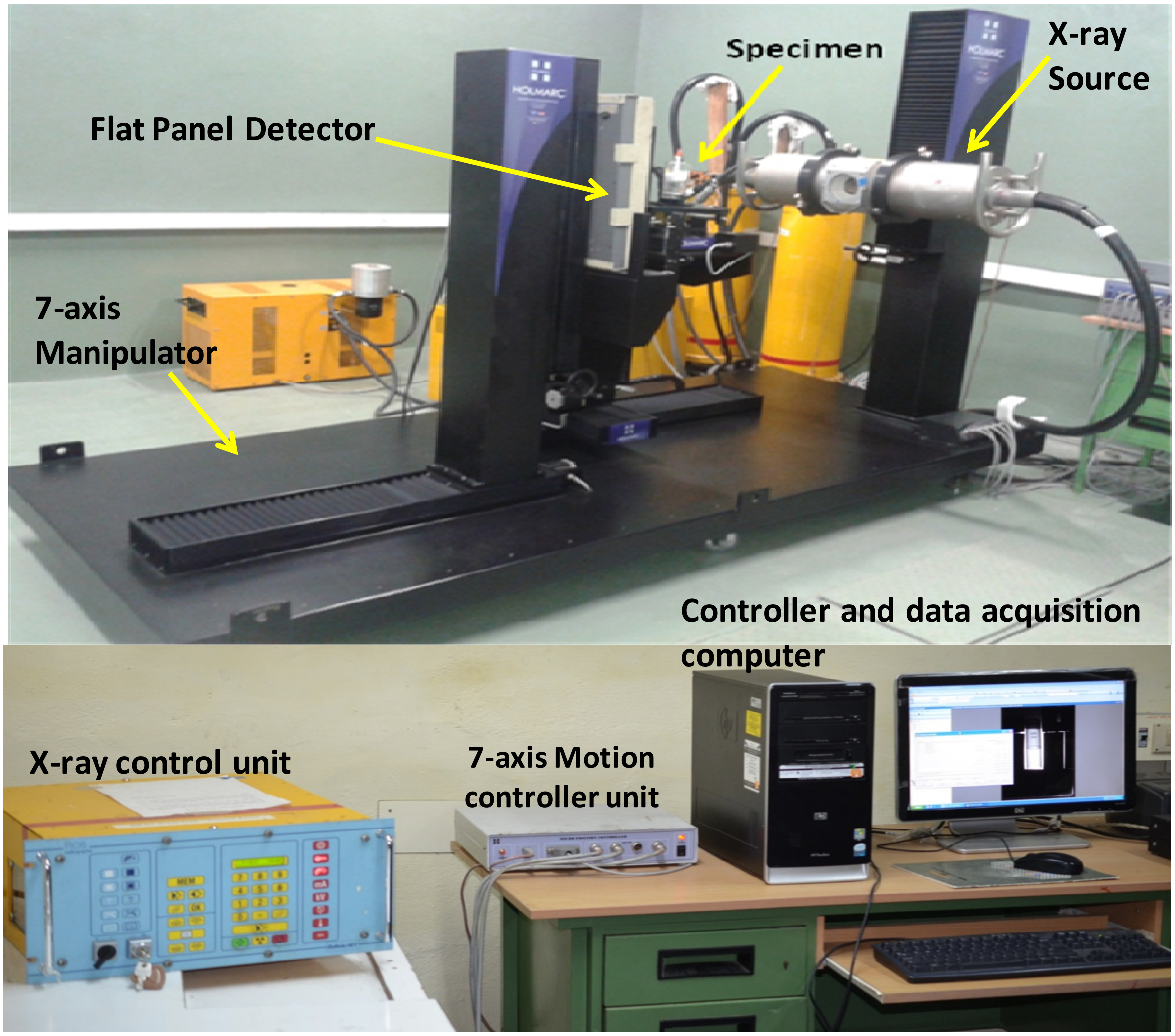

Fig. 2: Computed Tomography Experimental set up

A 450kV/20mA constant potential X-ray generator system with 1.2 mm and 3mm focal spot size is used for the experiment. The small focal spot was selected as it is smaller than the detector resolution. The anode voltage can be set in steps of 1kV and tube current can be set in steps of 1mA. The target material is tungsten and the 2mm Fe and 1mm Cu window which provides the inherent filtration of the beam. The specified radiation coverage is 40 degree. A high resolution digital X-ray flat panel based on a phosphor screen coupled to an array of amorphous silicon photodiodes and a-Si thin-film transistors (TFT) connecting the diodes to the readout electronics [24]. As the absorption efficiency of plain photodiode is not hgh enough for X-ray energies above 30-35keV, the most commonly used scintillators are gadolinium-based phosphor screens, CdWO4 and thallium-dopped CsI [25]. The a-Si array is processed on a monolithic glass substrate. The TFT and photodiodes are deposited using large area thin film semiconductor processes. The large size of this X-ray image sensor (28 cm x 40 cm), combined to a 127 µm square pixel, allows to use it where both high resolution and large field of view are needed. The front end electronic include pre-amplifying and multiplexing system including A/D converter, signal processing unit and frame grabber card interface. The 4-axis stepper motor controlled mechanical manipulator was used for object holding and alignment. There are two horizontal axis X-axis and Y-axis for bring the object in line with X-ray source and detector. The vertical axis Z-axis is for bringing the object inside the field of view. The rotator provides the specimen platform and rotates.

Table 1: Specification of the in-house developed CT-setup

Manipulator	**X-ray Source**	**Detector**	**Data Acquisition**
Span: X-ray Mounting stand: Z: 600mm Detector Mounting Stand: X: 700mm Z: 600mm Object Manipulation Stage: X: 400mm Y: 400mm Z: 100mm Θ: 360^0	**Beam :** Directional	**Screen:** Gd_2O_2S:Tb 127 microns	PCI – based frame grabber
Resolution: Linear: 10 micron Θ: 0.001 degree	**Voltage Range:** 10-200kV *(Seifert) 10-450kV #(Balteau)	**Active Area :** 2240 x 3200 ~ 7.1 million pixels	14 bit Analog-to-digital
Max. Wt.: 30Kg	**Max. Current:** *12mA #30mA	**Image readout :** FIFO	**Input :** Digital
Max. Diameter of the object : 150mm	**Max. Power:** *900W #4500W	**Read out time :** 4.2s	**PC :** 3 gigahertz Intel Core2 Duo

Motors: Stepper Motor	**Focal Spot Size:** *1.5mm air cooling #1.2mm and 3mm oil cooling	**Output :** Digital	**Memory :** 4G RAM
Make: Holmarc	**Make:** *(Seifert) #(Balteau)	**Make:** Thales FlashScan 35	**Make :** Matrox Imaging

The software is used for initiating and controlling scanning sequence and in particular consists of computer routine for (i) programming and controlling mechanical manipulator movement, (ii) programming linear array and data transfer and (iii) pre-processing X-ray measurements, display and processing. The pre-processing, image reconstruction, 2D and 3D visualization are developed in Matlab platform as shown in Fig. 3. The software has the facility to analyze the reconstructed grid values for statistical calculation and for graphical representation.

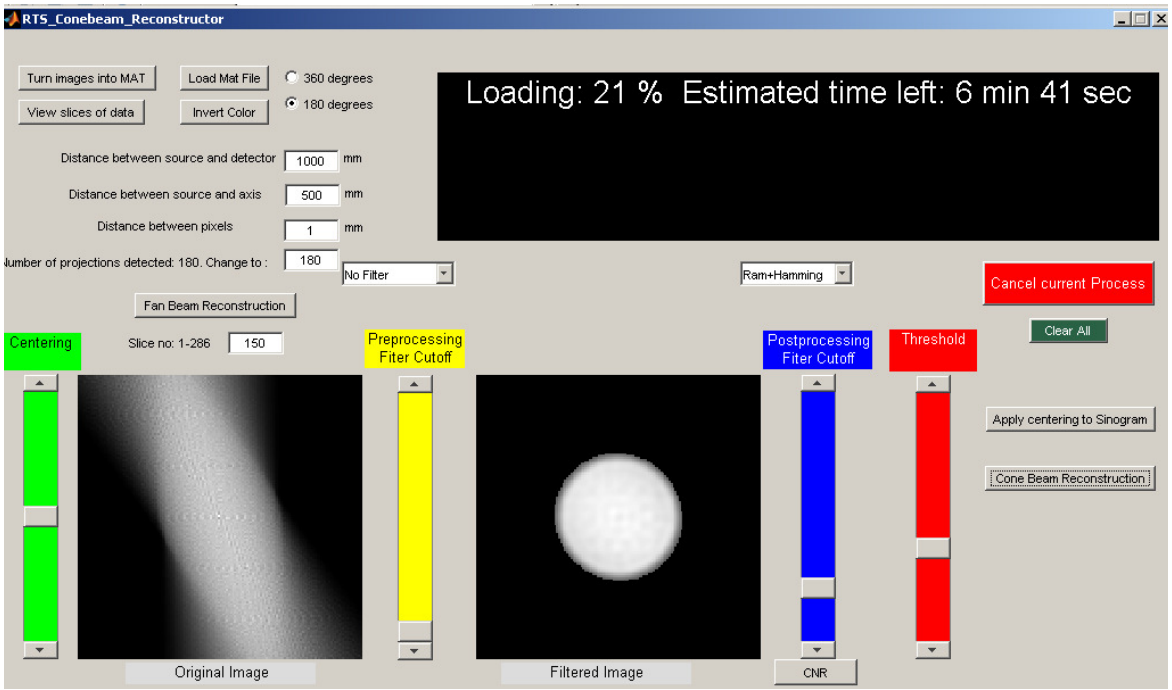

○ 360 degrees
● 180 degrees

Distance between source and detector 1000 mm
Distance between source and axis 500 mm
Distance between pixels 1 mm
umber of projections detected: 180. Change to : 180
No Filter
Ram+Hamming
Slice no: 1-286 150

Loading: 21 % Estimated time left: 6 min 41 sec

Fig. 3: CT reconstruction: MatLab Gui

4. Cone Beam Tomography applied to the quality control

3D Computed Tomography has been applied to the quality control focusing on two main aspects: Detection of flaws and dimensional measurements which includes the control of dimensions and the analysis of the deviation of the real geometry from the nominal geometry. In this paper we describe the application of CT setup at IGCAR to quality control of new developed materials. In the following sections we give a short impression of the application to motor stator for dimensional accuracy obtained for defect feature detections and sizing. By means of these investigation the materials, their composition and their behavior can also be analyzed and characterized. So the development of modern materials is also accelerated. The production process can be monitored and the process parameters can also be optimized.

4.1 3D visualization and dimensional analysis of a Stator Motor core specimen

Hence, a 3D visualization of stator motor core and studying any deviation in core cross section will help the fabricator to make corrective actions. The stator motor core is made of silicon steel (diameter 20mm and length 15mm) made by high speed stamping punches of 50 pieces (each piece is of thickness 0.3mm). The radiographic parameters are set as 1.5mm focal spot size, 140kV and 2mA exposure. At this radiographic parameters 180 projection data's were obtained at an angular interval of 1 degree, and the reconstruction was done using filtered back projection (FBP) technique. The interest of this study was to estimate the accuracy of reconstruction of various features like slot width, slot thickness and slot size in comparison to size measured using video microscope. The radiographic image of motor core, reconstructed cross-section and 3D image is shown in Fig. 4. The comparison of actual dimensions and measured by CT reconstruction is brought out in Table 2 and we can observe that a good accuracy of reconstruction is obtained [26-28].

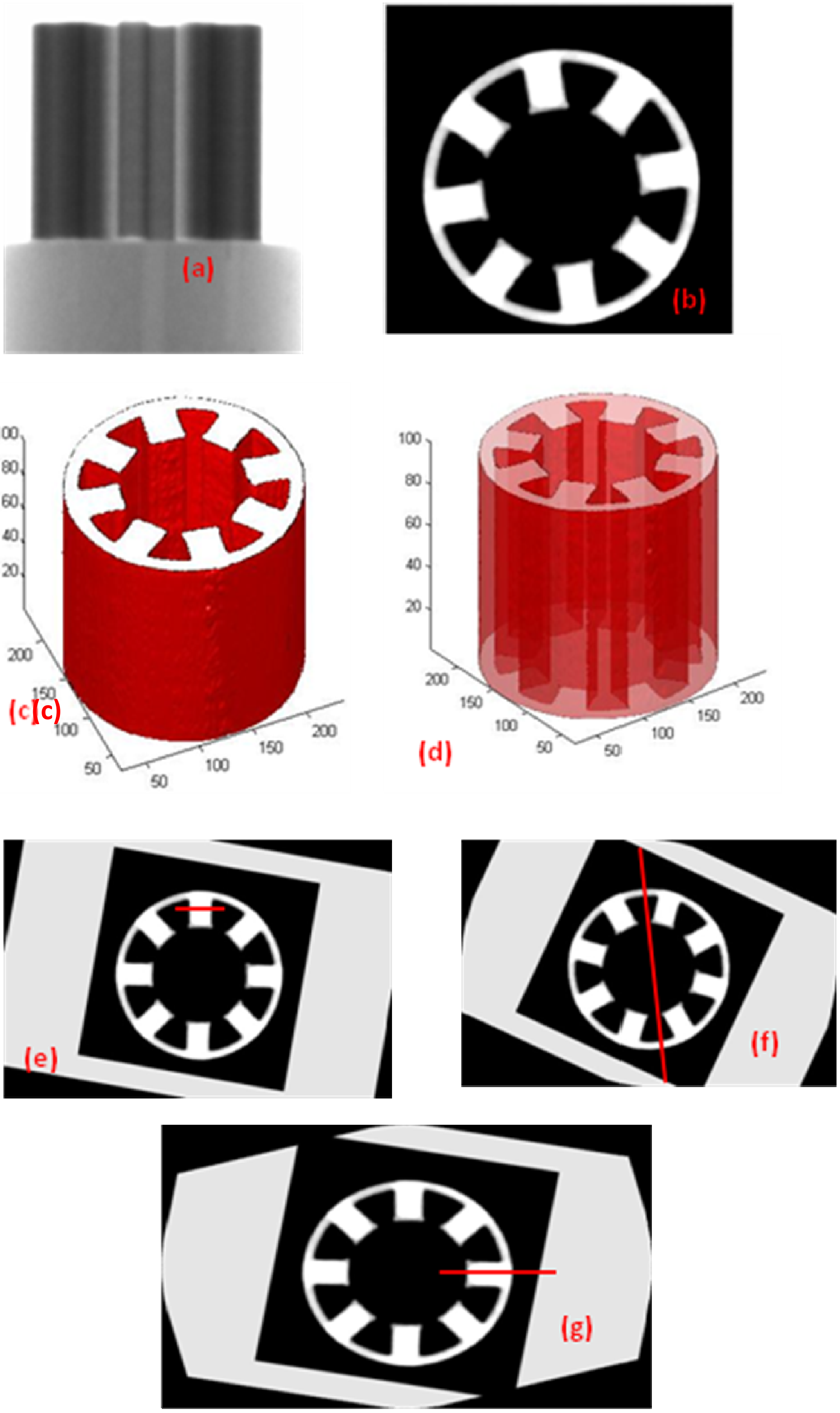

Fig. 4: a) Radiographic image of motor core b) reconstructed image c) 3D image (d) 3D image in transparent mode (e) quantification for slot width (f) quantification for thickness (g) quantification for slot breath.

Table 2: The percentage error in estimating the features sizes

Names	**Actual size measured using video microscope (in mm)**	**Measured (in mm) ±0.05mm**	**% Error**
Slot width	2.53	2.57	1.58%
Thickness	1.15	1.13	1.74%
Slot breath	4.39	4.32	1.59%

4.2 Visualization of Casting defects in Cast Ni-Al Bronze (NAB) alloy Fatigue specimen

The tensile specimen chosen is a copper-based quaternary alloy containing Ni, Al and Bronze (NAB) as the major alloying elements [29]. Excellent corrosion resistance, coupled with good tensile strength make it the material of choice for marine applications including propellers, pump impellers, pump casings, couplings, valves and sub-surface platforms. The casting procedure [30] leads to a complex microstructure because of the varying cooling rates associated with large castings which leads to a non-uniform microstructure that degrades the material properties and performance. During solidification and cooling gas evolution results in porosity, which further deteriorates the strength and corrosion resistance [29]. The defects that develop during casting process depend on factors such as materials, part design and processing techniques. The NAB alloy castings were procured in the form of blanks of dimensions, 25×25×110 mm. The chemical composition was determined using wet chemical analysis and is provided in Table 9. For conducting high cycle fatigue (HCF) tests, cylindrical specimens with a gauge length of 28 mm and a gauge diameter of 10 mm were machined from the cast NAB blanks as shown in Fig. 5.

Table 3. Chemical Composition of NAB (Weight Percent)

Element	Cu	Al	Ni	Fe	Mn	Mg	Si	Pb	Sn	Zn
Weight %	79.5	8.1	4.8	3.8	0.7	<0.02	0.1	0.1	0.1	0.6

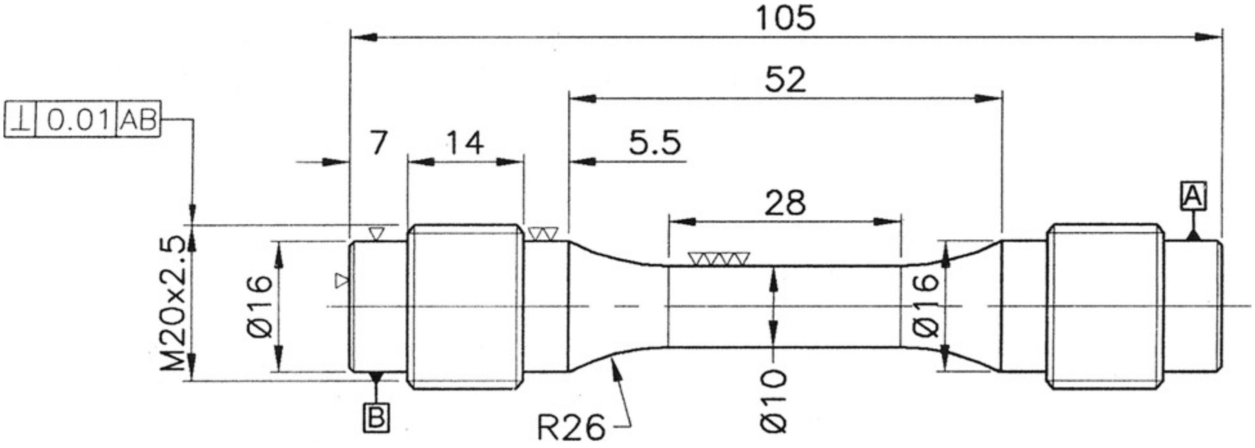

Fig. 5: Specimen geometry used for tensile test (dimensions in mm).

X-CT was carried out using a 450 kV Balteau constant potential X-ray tube and flash scan FS35 Thales flat panel X-ray detector with 127µm pixel sizes. To reduce the scattering from edge of the cylindrical shaped specimens, during radiography exposure the sample was inserted inside a 10mm thick shape correction block. The radiography exposure parameters used are given in Table 4. To estimate the sensitivity of RT measurements, stainless steel (SS) wire penetrameter ASTM 1-A (80, 100, 120, 160, 200, and 250 µm thick wires) was placed on the source side of the specimen. A sensitivity of 200 µm was achieved corresponding to 2% of wall thickness of the specimen.

RT and X-CT were carried out on the machined specimens before HCF testing to characterize the defects and to classify the specimens into various defect groups. From X-ray radiography, the nature and size of the defects were measured and X-CT was used to characterize the position of defect features present in the specimens.

Table 4: X-ray Radiographic and CT parameters

Radiographic parameters		CT parameters	
Focal spot (mm)	1.5	No. of projections obtained	181
kV	280	X Start, X End	1104,1422
mA	1	Y Start, Y End	1210,1580
SOD(mm)	1000	Zero pad data to slice	512
ODD(mm)	200	Center of projection data	156
Signal to noise ration (SNR)	170	Cross section slice required	256
		Steps of angular increments	1
		Zero pad FFT data to	1024

Thirty NAB specimens were classified into various defect groups based on the size of the defects. It was found that 4 out of the 30 specimens contained no casting defects viz. porosity, shrinkage cavities, etc. The defect size is expressed in terms of the range of defect radius for each individual defect group. The information's derived from the RT images cannot reveal the depth details of the defects detected. Hence, X-CT was carried out on selected specimens from each group for quantitative depth and exact shape and size of defects. The defects were categorized into the following groups and tabulated in Table 5:

(a) Non-defective
(b) Small defects
(c) Intermediate defects
(d) Large defects
(e) Surface defects

Table 5: Classification of NAB specimens into various defect groups

Sp. No	Class of defect	Range of Defect Diameter (in mm)	Specimen Nos.
1.	Non-defective		8, 20, 25, 28
2.	Small defects	1 - 2	5, 6, 7,11, 24, 26, 27,33, 34, 37, 38, 46
3.	Intermediate defects	2 - 3	12, 14, 39, 40, 41, 45
4.	Surface defects	1 - 2	13, 31, 35
5.	Large defects	3 - 4	1, 2, 10, 30, 44

3-D image segmentation was used for precise quantification of the size and morphology of the defects which in turn was used to calculate D_f for the different groups. Where D_f is expressed as a ratio of the defect area to the cross-sectional area within the gage length (78.25 mm^2), is tabulated in Table 6. The defect areas as shown in Figures 7(i), 8(i), and 9(i) are closely approximated to a circle for the all the defect groups.

a. **Non-defective:** No defects were observed in radiography images of this group and as an illustration radiography image of specimen No.8 is shown in Fig 6. This classification was deemed necessary as it would provide a baseline data for comparing the various defect groups.

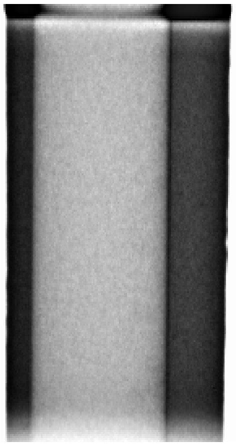

Fig. 6: Radiography image of Sp. No. 8 (Non-defective)

b. **Small defects:** The Radiography image of specimen No. 3 is shown in Figure 7(i). Analysis of the RT image shows that the number of defects vary in the range of 1-2 and have an average D_f of ~0.05. The number of defects in this category was found to be ranging from 1 to 2. The X-CT image as shown in Fig. 7(ii) gives an indication about the depth of the defect. From the profile plot of gray value vs. the distance from the surface in pixels, the porosity depth is measured approximately as 2 mm and radius 1 mm.

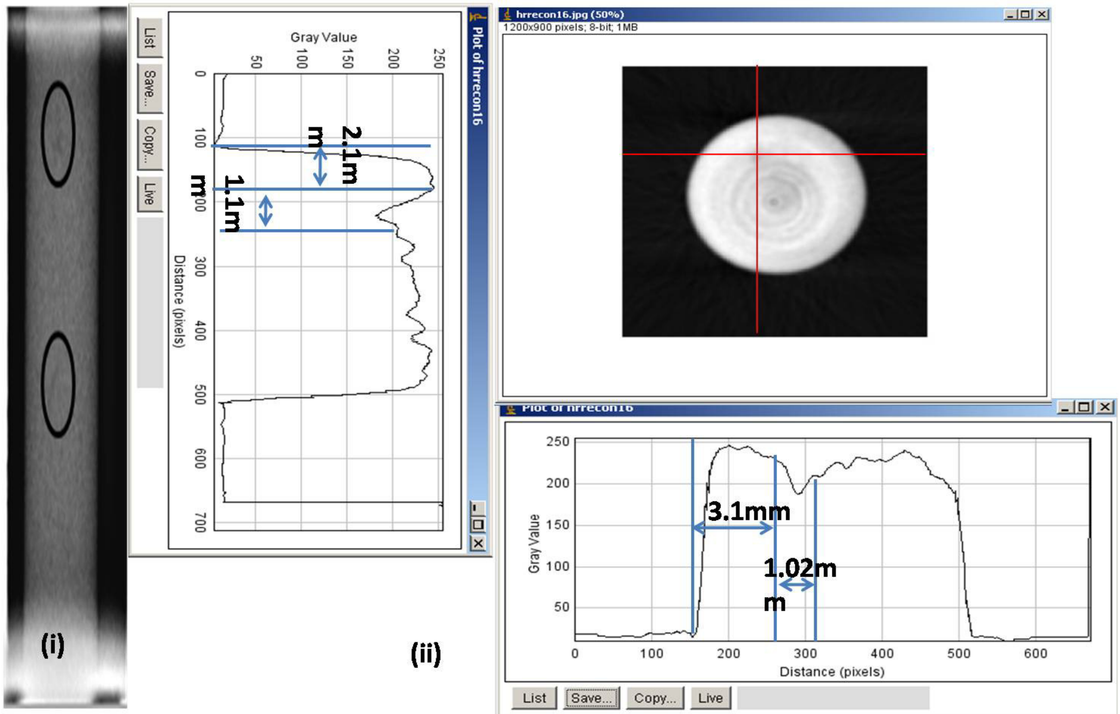

Fig. 7: (i) radiography images of Sp. No. 3 (Small defects), (ii) The cross-section of CT image along with gray-level profile plot for position of the defect

c. **Intermediate defects:** The radiography image of specimen No. 17(Fig. 8(i)) shows small clustered defects close to each other such that it appears as large defect and the average D_f for this group is ~0.25. The CT cross-section image shown in Figure 8(ii) indicates that the defects are very close to the outer surface. It is observed from the profile plot that the defects are approximately at a depth of 1.3 mm from the surface. The 3-D visualization image (Fig. 8 (iii)) generated using image J software shows clearly that the defects are very closely clustered.

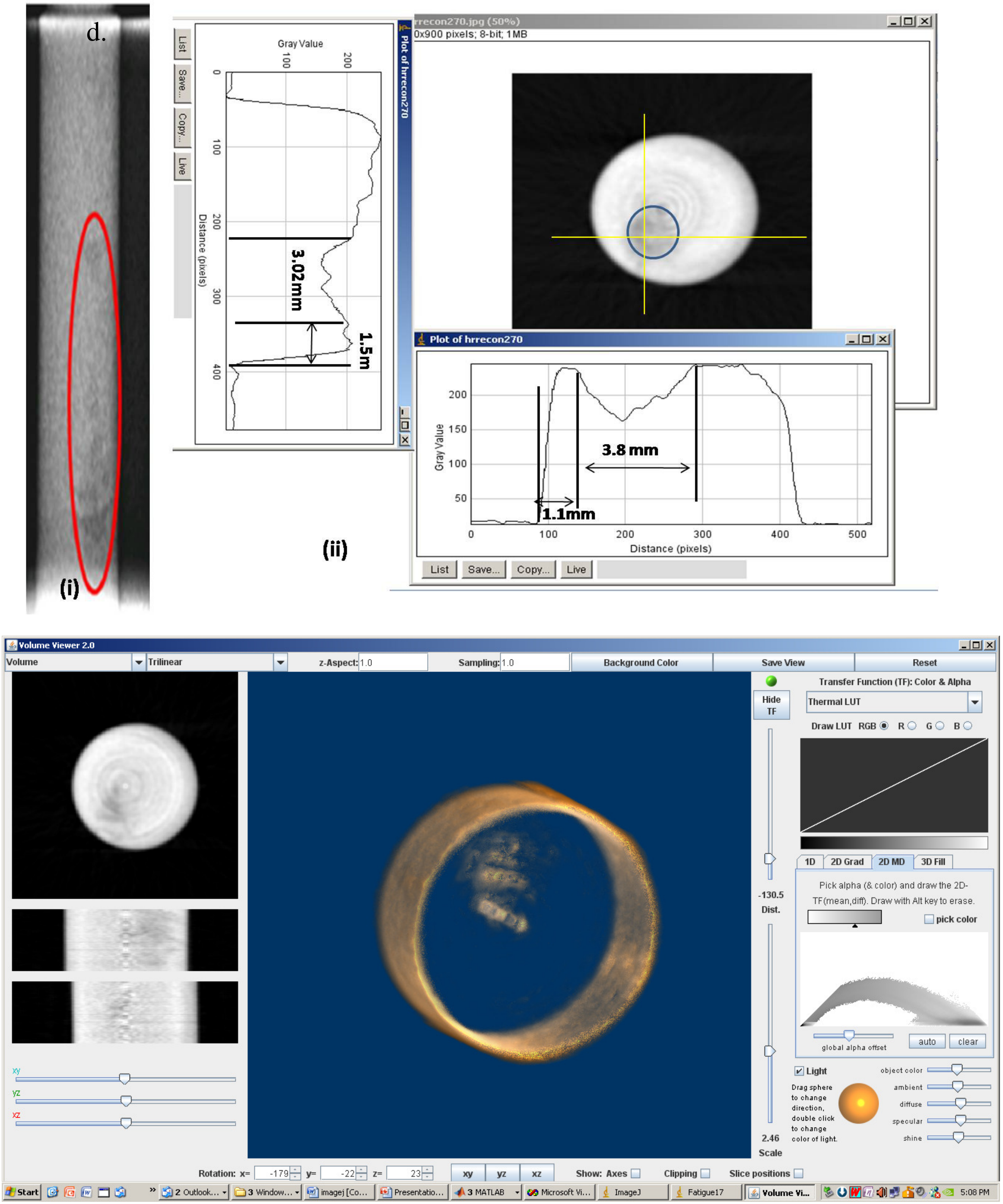

z-Aspect: 1.0
Sampling: 1.0
Thermal LUT
-130.5 Dist.
2.46 Scale
Rotation: x= -179 y= -22 z= 23

(iii)

Fig. 8: (i) radiography images of Sp. No. 17 (Intermediate defects), (ii) The cross-section of CT image and gray-level profile plot of the defect and (iii) 3-D visualization of the defects

e. **Large defects:** The large defects group radiography image of specimen No. 22 (Fig. 9(i)) has number of defects varying in the range of 1-3 and an average Df of ~0.4. Some of the defects size were comparable to intermediate defects but were not clustered instead they were joint. From the X-CT cross-section image (Fig. 9(ii)) the defects were also observed to be very close to or just below the surface. The gray-value plot showed that the defects are typically 1 mm below the surface and from the 3-D visualization images shown in Fig. 9(iii) we can observe that defects were joined and no clusters were noticed.

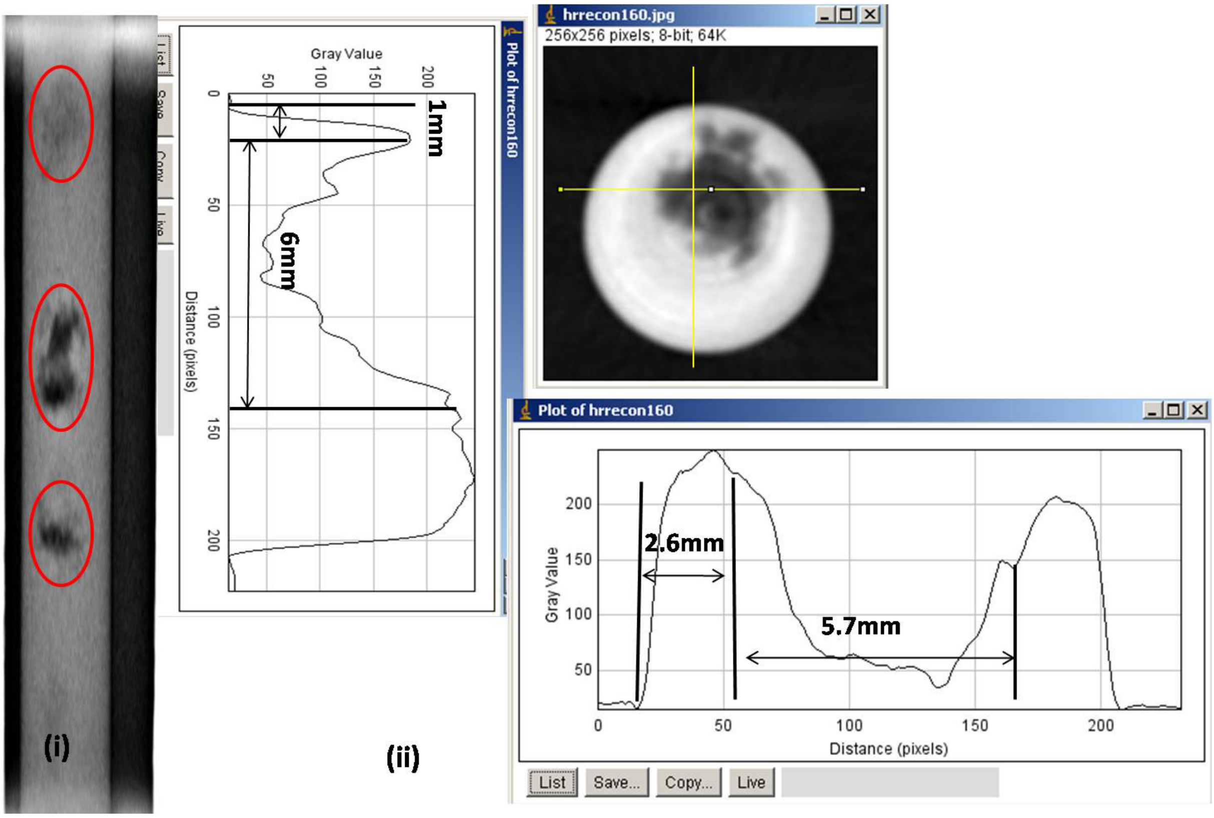

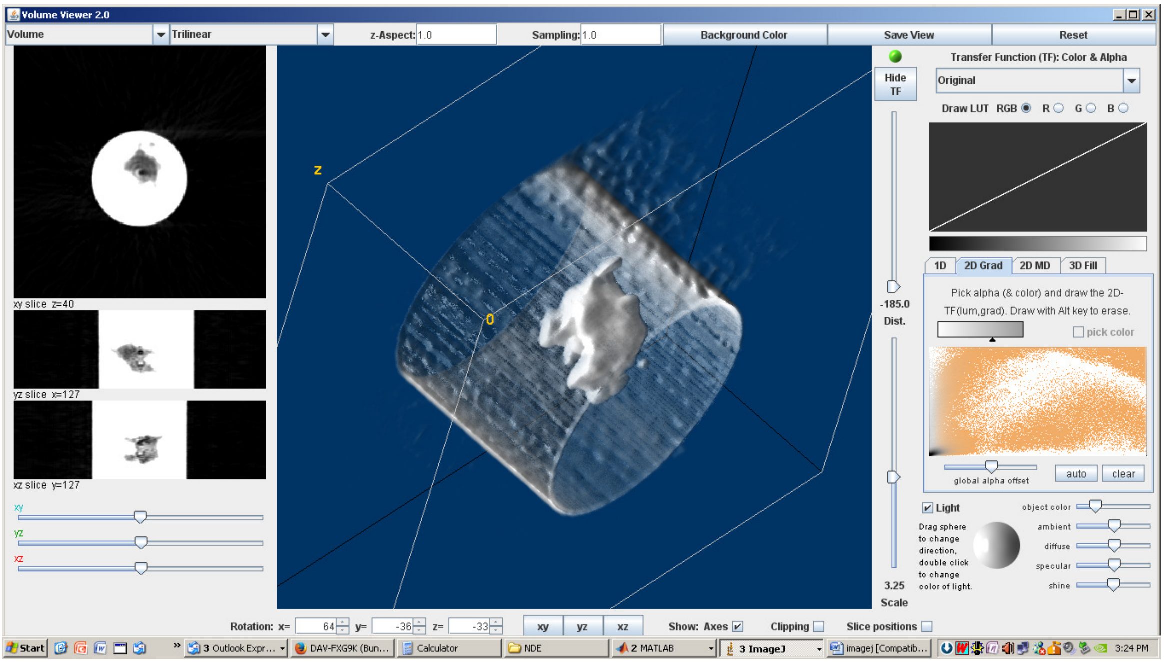

Volume Trilinear z-Aspect: 1.0 Sampling: 1.0

Transfer Function (TF): Color & Alpha: Original

Draw LUT RGB ● R ○ G ○ B ○

Pick alpha (& color) and draw the 2D-TF(lum,grad). Draw with Alt key to erase.

-185.0 Dist.

3.25 Scale

☑ Light

Drag sphere to change direction, double click to change color of light.

Rotation: x= 64 y= -36 z= -33

Show: Axes ☑ Clipping ☐ Slice positions ☐

(iii)

Fig. 9: (i) radiography images of Sp. No. 22 (Large defects), (ii) the cross-section of CT image and gray-level profile plot of the defect and (iii) 3-D visualization of the defects

e. **Surface defects:** These are specimens with visible surface defects and radiography image of specimen No. 35 is shown in Fig. 10(i). The X-CT image cross-section in Fig. 10(ii) clearly shows the surface opening and depth of the defect. The gray level plot to show the depth of the surface defect typically 4.2mm and 3-D image presented in Figure 10(iii).

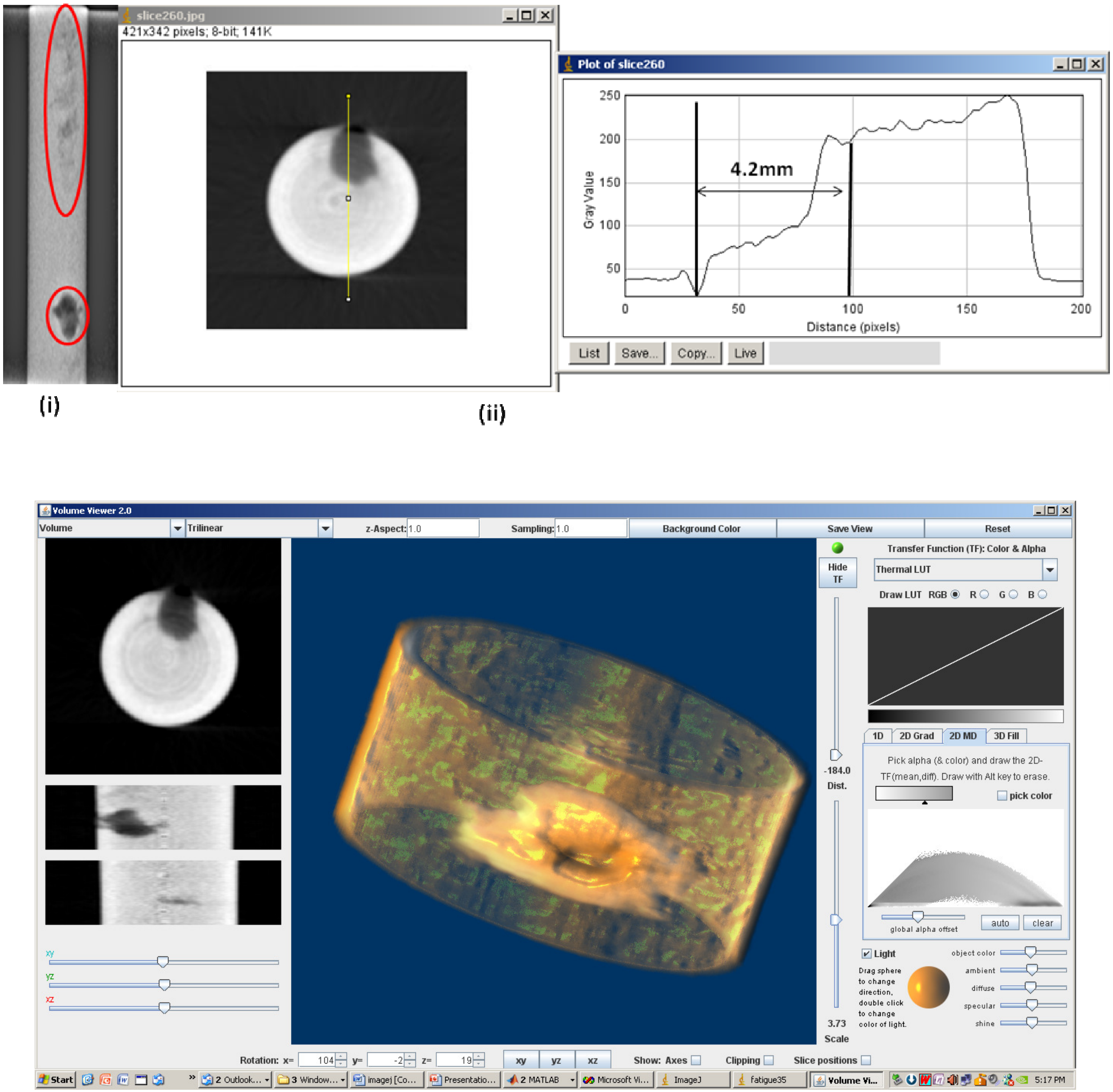

slice260.jpg

421x342 pixels; 8-bit; 141K

Volume Viewer 2.0

Volume, Trilinear, z-Aspect: 1.0, Sampling: 1.0

Transfer Function (TF): Color & Alpha: Thermal LUT

Draw LUT: RGB ●

Rotation: x= 104 y= -2 z= 19

(iii)

Fig. 10: (i) radiography images of Sp. No. 35 (Surface defects), (ii) the cross-section of CT image and gray-level profile plot of the defect and (iii) 3-D visualization of the defects

Table 6: Defect fraction calculation

S. No	Defect Groups	Radius of defect (in mm)	Area of the defect Circle (mm^2)	Defect fraction (D_f)	Average Defect fraction (D_f)
1	Small defects (Fig. 4 (b) (i))	1.27	5.024	0.064	0.05
		1.17	4.299	0.055	
2	Intermediate defects (Fig. 4 (c) (i))	2.53	20.096	0.257	0.25
		2.37	17.663	0.226	
3	Large defects (Fig. 4 (d) (i))	3.16	31.4	0.401	0.4
		3.16	31.4	0.401	
4	Surface defects (Fig. 4 (e) ((i))	1.58	7.85	0.1	0.3
		2.21	15.386	0.197	

5 Conclusions

The cone beam tomographic system at IGCAR is a versatile tool for quality control in view of a rapid development of new products with new materials. The system allows a fast tomographic volume scanning as well as a high spatial resolution in all 3 directions. With a single NDT tool and a single measurement, defects in complex bodies can be detected and analyzed regarding their 3D shape, orientation and position. Dimensional measurements of outer and inner structures can be performed to verify the geometry of parts. For accurate dimensional measurement the method of correcting CT data by using reference standard object is presented here. The stator motor core is considered as a reference object and the accuracy of reconstruction of feature dimension was ~ 98%. Based on CT analysis, the casting defects observed in as-cast NAB alloy were sub-divided into different defect groups having particular defect size and defect locations. The groups were broadly classified as follows: (a) Non-defective, (b) Small defects (~1mm), (c) Intermediate defects (~2mm), (d) Large defects (~3mm), and (e) Surface defects.

6 Reference

1. CM Sonsino, J Ziese, “Fatigue strength and applications of cast aluminum alloys with different degree of porosity”, Int. J. Fatigue, Vol.15, pp.75–84, 1993.
2. MJ Couper, AE Neeson, JR Griffiths, “Casting defects and the fatigue behavior of an aluminum casting alloy”, Fatigue Fract. Eng. Mater. Struct., Vo. 13(3), pp. 213–27, 1990.
3. YX Gao, JZ Yi, PD Lee, HM Flower, TC Lindley, “The effect of porosity on the fatigue life of cast aluminium–silicon alloys”, Fatigue Fract. Eng. Mater. Struct., Vol. 27, pp. 559–70,2004.
4. QG Wang, D Apelian, DA Lados, “Fatigue behavior of A356-T6 aluminum cast Alloys - Part I Effect of casting defects”, J. Light Metals, Vol.1, pp. 73–84, 2001.
5. P Clement, J Angeli, A Pineau, “Short crack behaviour in nodular cast iron”, Fatigue Fract. Eng. Mater. Struct., Vol.7(4), pp. 251–65, 1984.
6. K Tokaji, T Ogawa, “Fatigue life distribution and its simulation in spheroidal graphite cast irons”, Int. J. Fatigue, Vol.19 (8), pp.662, 1997.
7. H Yaacoub Agha, A Béranger, R Billardon, F Hild, “High-cycle fatigue behavior of spheroidal graphite cast iron”, Fatigue Fract. Eng. Mater. Struct., Vol. 21(3), pp. 287–96, 1998.
8. Y Murakami, “Metal fatigue: effects of small defects and nonmetallic inclusions”, Elsevier, 2002.
9. EN 1369:1997, Founding – magnetic particle inspection. CEN; July, 1997.
10. EN 12680-3:2003, Founding – ultrasonic examination, part 3: spheroidal graphite cast iron castings. CEN; August, 2003.
11. Baldev Raj, T. Jayakumar and M. Thavasimuthu, “Practical Non-destructive Testing”, 2nd Edition, Woodhead Publishing Limitied, 2002.
12. Baldev Raj and B. Venkataraman, “Practical Radiography”, Narosa Publishing House and National Certification Board of Indian Society for Nondestructive Testing, 2007.
13. E Ferrie, JY Buffiere, W Ludwig, “3D characterization of the nucleation of a short fatigue crack at a pore in a cast Al alloy using high resolution synchrotron microtomography”, Int. J. Fatigue, Vol. 27, pp. 1215–20, 2005.

14. C Verdu, J Adrien, JY Buffiere, “Three-dimensional shape of the early stages of fatigue cracks nucleated in nodular cast iron”, Mater. Sci. Eng. A, Vol. 483, pp. 402–5, 2008.
15. Powazka P et al., “Computed tomography – an alternative and complement to traditional metallographic investigations of porosity in cast aluminum”, In: Procs. of 2nd fatigue symp., Leoben, pp. 51–66, 2008.
16. Matin Simon, Christoph Sauerwein, Ion Tiseanu, Sandrine Burdairon, “Multi Purpose 3D Computer Tomography System”, Proceedings of the 8th European Conference on Non-Destructive Testing, Barcelona, 2002.
17. Matin Simon and Christoph Sauerwein, “Cone Beam Tomography for Quality Control and Rapid Product Development”, Insight, Vol. 42, No.10 , pp. 651- 655, 2000.
18. Sture Persson and Erik Ostmant, “The Use of Computed Tomography in Non-destructive Testing of Polymeric Materials, Aiuminium and Concrete: Part 2---Applications”, Polymer Testing, 6, pp. 415-446, 1986.
19. V Jandhyala, N Dasgupta, “Characterization of air void distribution in asphalt mixes using X-ray computed tomography”, J. Mater. Civil Eng., Vol. 14, pp. 122, 2002.
20. T Marrow, J Buffiere, P Withers, G Johnson, D Engelberg, “High resolution X-ray tomography of short fatigue crack nucleation in austempered ductile cast iron”, Int. J. Fatigue, Vol. 26(7), pp. 717–25, 2004.
21. Herman, G.: Image Reconstruction from Projections. The Fundamentals of Computerized Tomography. Academic Press 1980.
22. F. Natterer : The Mathematics of Computerized Tomography. Wiley-Teubner 1986. (New York: John Wiley & Sons)
23. Kak, A.C.-Slaney, M: Principle of Computerized Tomography Imaging. IEEE Press 1987.
24. R.L.Weisfield, M.Hartney, R.Schneider,K.Aflatooni, R.Lujan, "High Performance Amorphous Silicon Image Sensor for X-ray Diagnostic Medical Imaging Applications", SPIE Medical Imaging, Vol. 3659, No.1, pp. 307-317, 1999.
25. Umesh Kumar, G. S. Ramakrishnan, A. S. Pendharkar and Gursharan Singh, “Behaviour of reconstructed attenuation values with X-ray tube voltage in an experimental third-generation industrial CT system using Xscnan linear detector array”, Nuclear Instruments and Methods in Physics Research A, 490, pp. 379-391, 2002.

26. M. Bartscher, U. Hilpert, J. Goebbels, G. Weidemann, “Enhancement and Proof of Accuracy of Industrial Computed Tomography (CT) Measurements”, Annals of the CIRP Vol. 56/1/2007, pp. 495-498.
27. J. Hofmann, A. Flisch, “A wall-thickness-based method of adaptive integration time determination for X-ray computed tomography”, NDT&E International 39 (2006) 668–674.
28. Fiorello losano, Gabriella Marinsek, Alberto Maria Merlo, Miriam Ricci, “Computed Tomography in automotive field development of a new engine head case study”, Computerized tomography for industrial applications and image processing in Radiology, March 15-17, 1999, Berlin, Germany, pp. 65-73.
29. W.A. Nabach: The Effects of Isothermal Deformation and Annealing on the Microstructure of NAB Propeller Material, Naval Post Graduate School, US Navy, 2003.
30. ‘‘Standard Specification for Aluminium-Bronze Sand Castings’’, ASTM, B-148-97 (Reapproved 2009).